Experimental and numerical investigation of an autonomous flap for load alleviation

Bernhammer, Lars; Navalkar, Sachin; Sodja, Jurij; De Breuker, Roeland; Karpel, M

DOI
10.2514/1.C033767

Publication date
2017

Document Version
Accepted author manuscript

Published in
Journal of Aircraft: devoted to aeronautical science and technology

Citation (APA)
Bernhammer, L., Navalkar, S., Sodja, J., De Breuker, R., & Karpel, M. (2017). Experimental and numerical investigation of an autonomous flap for load alleviation. *Journal of Aircraft: devoted to aeronautical science and technology*, *54*(2), 464-475. https://doi.org/10.2514/1.C033767

This is an Accepted Manuscript of an article published in: Journal of Aircraft
Vol. 54 no. 2, pp. 464-475
Available online: https://doi.org/10.2514/1.C033767

Experimental and Numerical Investigation of an Autonomous Flap for Load Alleviation

Lars O. Bernhammer*, Sachin T. Navalkar †, Jurij Sodja ‡, and Roeland De Breuker§
Delft University of Technology, Delft, 2629HS, The Netherlands

Moti Karpel¶
Technion Israel Institute of Technology, Haifa, 32000, Israel

This paper presents the design, a numerical aeroservoelastic investigation and experimental proof of concept of an autonomous flap system. Autonomous flaps are load alleviation devices, which can be installed on any existing structure, for example wings or wind turbine blades, as plug-and-play unit. An autonomous flap system, which is integrated into a free-floating flap actuated by a trailing edge tab, consists of actuators, sensors, and a controller. Such a system is self-sufficient as it generates sufficient energy by harvesting the energy of mechanical vibrations. The energy harvesting process is particular efficient, when the wing-flap system starts to flutter, which is then transformed into limit cycle oscillations (LCO) using the control system or structural delimiters. It has been shown experimentally and numerically that the autonomous flap system, when mounted in an aeroelastic apparatus, flutters at low wind speeds. Stable, high-amplitude limit cycle oscillations were achieved during a wind tunnel experiment by limiting the amplitude of the flap deflections, while low-amplitude limit cycles could be reached by control activity. The autonomous flap system, when in controlled LCO, has a positive energy balance, such that it can be indeed used as autonomous device.

Keywords: Autonomous Flap, Energy Harvesting, Experimental Aeroelasticity, Limit Cycle Oscillation

I. Introduction

Gust loads are among the driving loads in the design of wind turbine blades and aircraft wings. The transient response due to a gust can be reduced by actively controlling the aerodynamic properties of a wing or airfoil section, for example by deforming the trailing edge of the airfoils. An option to achieve this deformation is to integrate a discrete flap into the wing structure. One of the flap concepts, which has been proposed, is a free-floating flap (FFF), which is driven by a trailing edge tab. Heinze and Karpel[1] were the first to introduce such a flap concept in their study of control applications of highly flexible wings. Bernhammer et al.[2] have further worked out this concept by showing the capabilities of the FFF as load alleviation and gust suppression device. Pustilnik and Karpel[3,4] studied the limit cycle behavior of the free-floating flap concept due to free-play in the actuator connection. The system flutters within the free-play zone and the limit cycles are reached by structural stiffness outside of the free-play zone.

The free-floating flap has been proposed as a load alleviation device for aircraft wings or propeller blades. With the aim of increased modularity, an autonomous flap combines the functionality of such a flap with an energy harvester. In the case of the autonomous flap, energy harvesting is achieved by converting vibrations, which are introduced by the aeroelastic response of the wing to turbulence and gusts, into electrical energy. Energy harvesting exploting the aeroelastic characteristics is a developing research field. The ground work

*PhD Candidate, Aerospace Structures and Computational Mechanics/ Wind Energy
†PhD Candidate, Delft Center for Systems and Control
‡Aerospace Structures and Computational Mechanics
§Assistant Professor, Aerospace Structures and Computational Mechanics
¶Professor, Sanford Kaplan Chair for Aerospace Engineering, Fellow AIAA

has been done by Bryant et al.[5,6] who use a cantilevered piezoelectric bender with a free-floating flap at its trailing edge. The system is operated in flutter conditions. Park et al.[7,8] use electromagnetic energy conversion instead of piezoelectric devices. In their experiment, a T-shaped cantilevered beam sheds vortices, thereby causing the beam to flutter. Bruni et al.[9] have studied the effect of aeroelastic instabilities on energy harvesting by using embedded piezoelectric elements. Sirohi et al.[10] also use embedded piezoelectric patches to harvest electrical energy from mechanical vibrations of a galloping triangular bar attached to a cantilever beam.

Bernhammer et al.[11] have demonstrate that such an harvesting system can be directly integrated into a wing-flap structure, similar to a vertical tail plane. While previous work showed the feasibility of load alleviation and energy harvesting individually,[2,11] this paper describes a proof-of-concept experiment of a complete autonomous system.

The paper is divided into a design, a numerical and an experimental part. First, the physical design of a wind tunnel demonstrator is presented. Then the time-domain response of the system is predicted using a numerical simulation. Special attention is devoted to the controller design, which is the most critical component in the autonomous flap as it needs to switch between harvesting and control modes. The experimental set-up is explained and the experimental results shown. Finally, these are compared to the numerical prediction of the autonomous flap system.

II. Aeroelastic Design of an Autonomous Flap

The Autonomous flap combines the functionality of a free-floating flap with an energy harvester. The proposed concept is detailed in Figures 1 and 2. The flap is the top level component, which contains all subcomponents such as sensors, a control system, actuators, an energy harvesting device and the trailing edge tab. The most significant advantage of the autonomous flap is that it is a completely autonomous system, meaning that no connection to the wing structure is needed other than a structural attachment. Hence, it can be used as a plug-and-play device on existing structures.

Accelerometers were used in this paper to measure the motion of the wing-flap system. As shown in Figure 2 the accelerometer should be mounted as close to the rotational axis of the flap as possible in order for the wing plunge motion to dominate the measured acceleration response. The obtained signal is used as input to a controller, which has been designed based on an experimental system identification of the autonomous, free-floating flap in the aeroelastic apparatus. Depending on the input, the controller sets the deflection angle of the trailing edge tab by commanding the actuator. Therewith, an aerodynamic moment is generated by the trailing edge tab that rotates the flap. This flap deflection creates an aerodynamic force that can be used for controlling the entire structure.

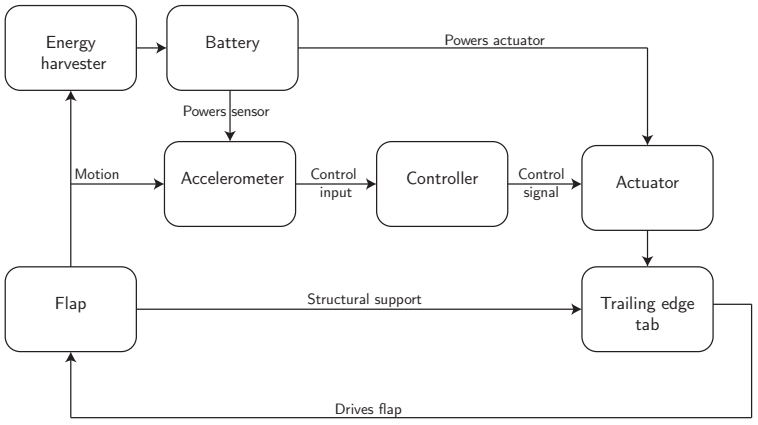

Figure 1. Flow chart of the autonomous flap concept[11]

The sensors, the control system and the actuation system are powered by electromagnetically harvesting the energy of aeroelastic vibrations. As has been shown by Bernhammer et al.,[11] the power generation is particularly effective when the system is aeroelastically unstable. Therefore, it is highly desirable to generate controlled oscillations that can provide continuous power production without being destructive for

the structure. A potential solution is to constrain the unstable oscillations to remain within acceptable limits (Limit Cycle Oscillations (LCO)). The amplitude of such oscillations can be limited either passively using structural delimiters or actively by a controller.

Close to flutter speed the inertia of the flap is reduced due to unsteady aerodynamic forces. Consequently the flap can be effectively controlled by a small trailing edge tab which, translated into control terminology, increases the effective control authority of the tab deflections[2,11] which in turn results in diminished power requirements in order to control such a system.

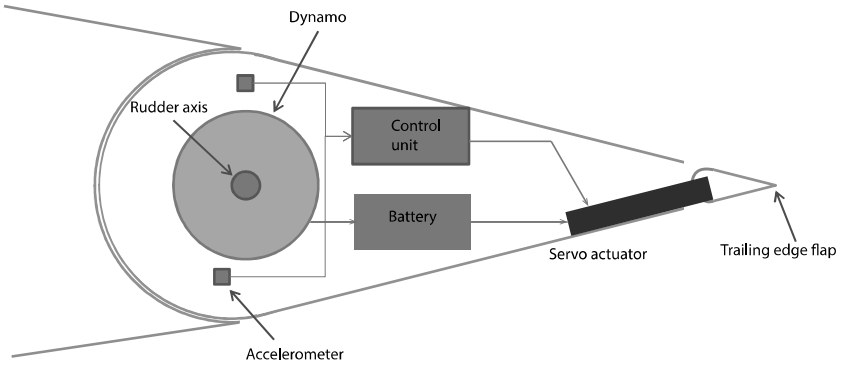

Figure 2. Schematic build-up of an autonomous flap[11]

III. Aeroelastic Test Set-Up

A. Wind Tunnel Set-up for Oscillating Airfoils

The autonomous, free-floating flap concept has been integrated in an aeroelastic apparatus consisting of a wing section that can undergo pitch and plunge motion. This test set-up has been originally constructed for aeroelastic validation experiments for CFD simulations[12] and modified to incorporate the autonomous flap system. The aeroelastic apparatus is displayed in Figure 3. The wing section (F) is attached by springs to the side walls (C) which are connected by beams (D) in order to form a rigid frame. This frame is mounted on a table (B), which can be adjusted to the height of the jet exit of the open test section (A). Struts (E) on both sides are used to increase the stiffness of the frame. Plunge and pitch motion of the wing section are decoupled by having a global translating system (I), on which rotational springs are mounted as shown in Figure 4. The side plates are guided by a rail system to prevent motion other than pure plunge. The springs (H) are attached to load cells and the side plates (I) are equipped with angular sensors and accelerometers. Strain gauges are attached to the root of the wing section. The properties of this set-up are given in Table 1.

Table 1. Properties of the aeroelastic set-up

Width	1800 mm
Chord	500 mm
Airfoil profile	DU96-W-180
Flap chord	100 mm
Plunge spring stiffness	8225 N/m^2
Structural damping	77.9 kg/s
Wing assembly mass	22.7 kg
Wing mass	15.2 kg
Side plate mass	7.5 kg
Eigenfrequency	3.0 Hz

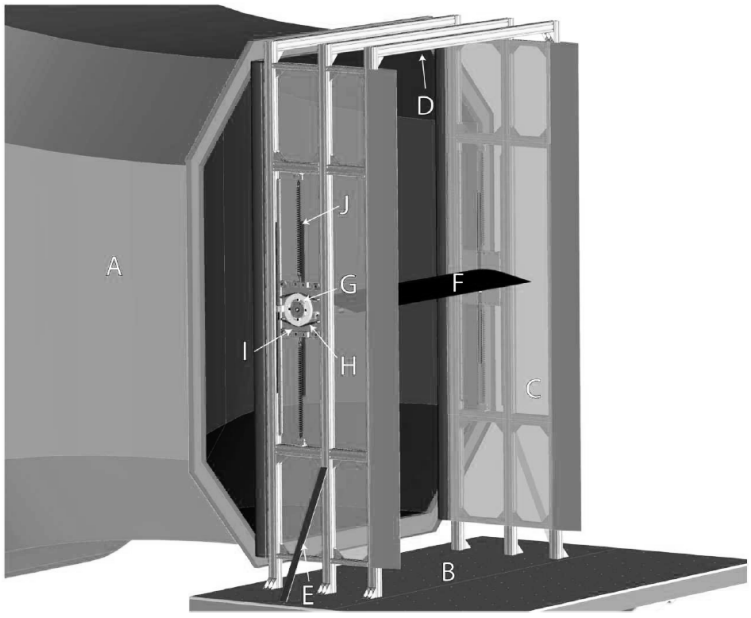

Figure 3. Experimental set-up in the open jet facility: the jet exit (A), the table (B), two sides upright (C), connecting beams (D), struts (E) and the wing section (F). Moment sensors (G) are attached to springs (H) on movable side plates (I)[12]

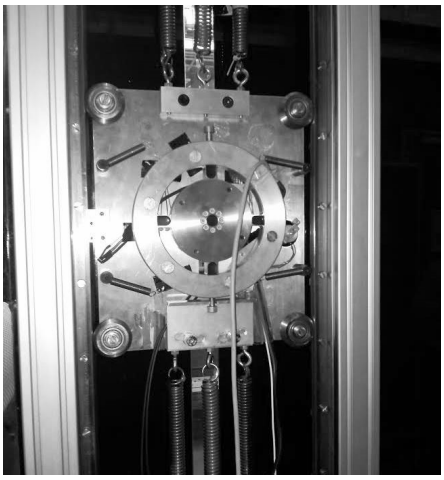

Figure 4. Side plate with plunge-pitch mechanism

B. Autonomous Flap Model

Table 2 provides an overview of the equipment that has been installed in the autonomous flap. The arrangement of all components in the flap is shown in Figure 5. The accelerometer (A) measures motion in the plunge direction. The potentiometers (B) and the gearboxes (C) are used to track rotation and transfer rotational motion of the flap to the electric generator. They are also used to hinge the flap to the wing. The gear box is connected to a generator. A pair of servo-motors (D) drives the trailing edge tab (E).

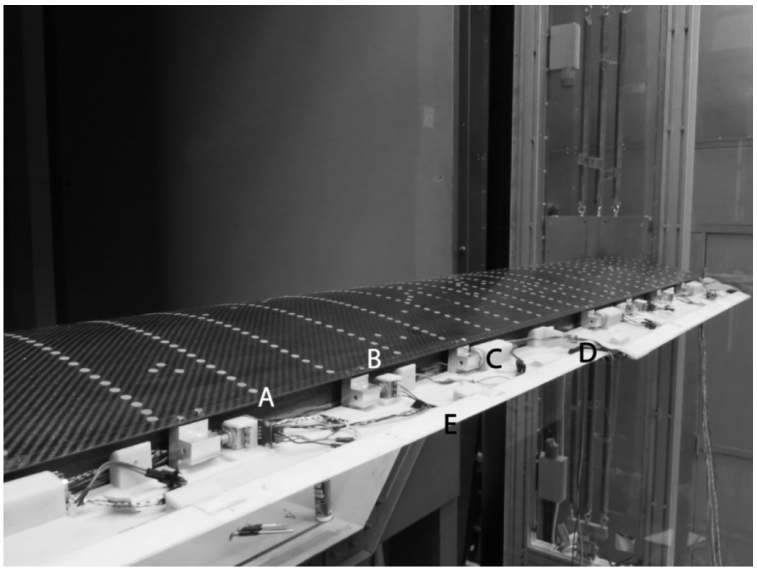

(a) Wind tunnel set-up

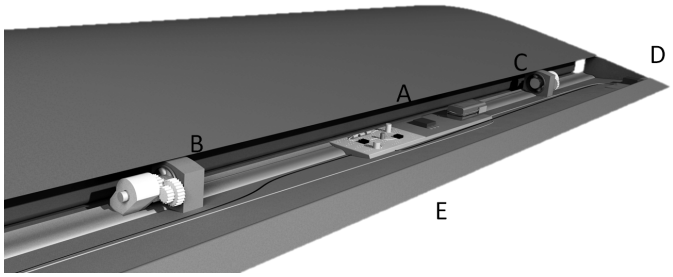

(b) Catia drawing

Figure 5. Autonomous free-floating flap with active trailing edge

C. Aeroelastic Analysis

As a first step, a flutter analysis was performed. It is very critical to operate close to the flutter speed as both the control authority of the trailing edge tabs and the power generation increase close to the flutter speed as was shown by Bernhammer et al.[2,11] The flutter analysis was done in MSC/Nastran using the PK-method.[13] Figure 6 shows the relevant aeroelastic modes. The frequencies in the caption of Figure 6 correspond to the natural frequencies of the test setup without aerodynamic forces. The first two modes are rigid-body modes of the free-floating flap at 0.0 Hz. The third eigenmode is a plunge dominated mode at 3.0 Hz, which also has a flap deflection component. The fourth mode of the wing section is a torsion dominated mode with a frequency of 6.8 Hz. All other elastic modes are clearly separated from the first four modes in terms of frequency; their frequencies are more than an order of magnitude higher.

Table 2. Flap design parameters

Material	SL-Tool STONElike
Density	1.37 g/cm^3
Young's modulus	3.5 GPa
Tensile strength	47 MPa
Skin thickness	2 mm
Servo actuator	HiTech HS-7115TH
Gear box	Apyxdyna AM022
Gear ratio	1:80
Generator	Kinetron MG 23.0
Analogue devices	ADXL78

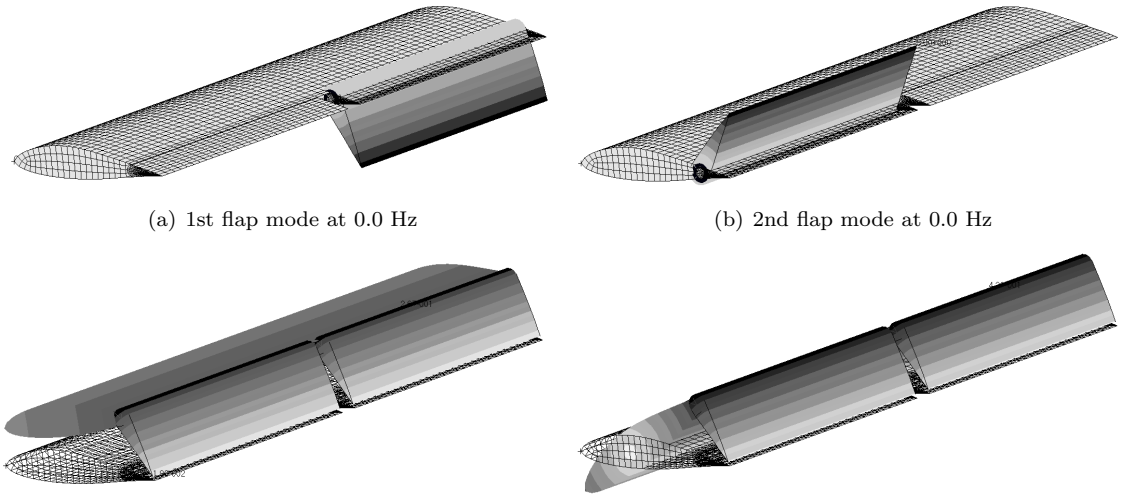

(a) 1st flap mode at 0.0 Hz

(b) 2nd flap mode at 0.0 Hz

(c) 1st plunge mode at 3.0 Hz

(d) 1st pitch mode at 6.8 Hz

Figure 6. Structural modes

The frequency and damping plots of the aeroelastic system are shown in Figure 7. The frequencies of the two flap modes increase almost linearly with the increasing wind speed, because aerodynamic stiffness is added to the flap deflection modes. The flap deflection curve with the higher slope corresponds to a synchronous vibration of the two flaps, whereas the curve with the smaller slope corresponds to a 180 degrees phase difference between the two flaps. Both modes are highly damped. While the frequency of both flap deflection modes increases quickly with the velocity, the frequency of the plunge mode is constant up to 8.0 m/s. From that velocity onwards, interaction of the plunge mode with the synchronous flap deflection mode takes place and the damping of the plunge mode reduces until flutter occurs at a velocity of 11.0 m/s. Figure 8 shows four snapshots over a half-cycle of the unstable plunge mode at the flutter speed.

The frequency of the pitching mode hardly changes in the velocity window of the experiment up to 16.0 m/s. Around 30.0 m/s the frequency of the plunge mode drops from the natural frequency of 6.8 Hz to 5.0 Hz. At this point interaction with the plunge mode takes place, which has a frequency of 3.7 Hz. Both modes approach each other rapidly in terms of frequency until they have the same frequency of 4.2 Hz at 40.0 m/s. This plunge-pitch type of flutter is however outside the scope of the investigation.

The mode shapes as obtained using MSC/Nastran have been used as basis for an aeroelastic analysis in ZAERO.[14] ZAERO has been used to obtain a state-space representation of the aeroelastic plant, which is used in the time domain simulations of the autonomous flap system. The transfer functions between accelerometers and tab deflection angle have been examined using the resulting state-space models for a velocity of 10.0 m/s. The Bode plots are given in Figure 9. The eigenfrequencies of both the plunge and the

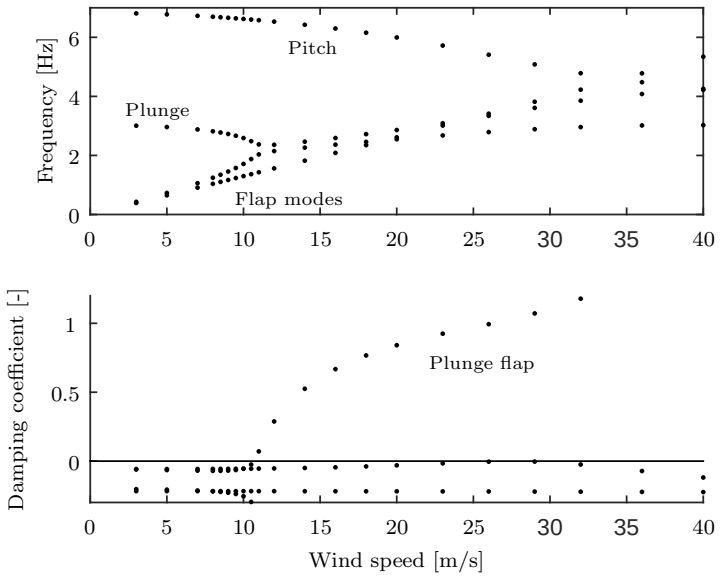

Figure 7. Damping and frequency plots as function of velocity

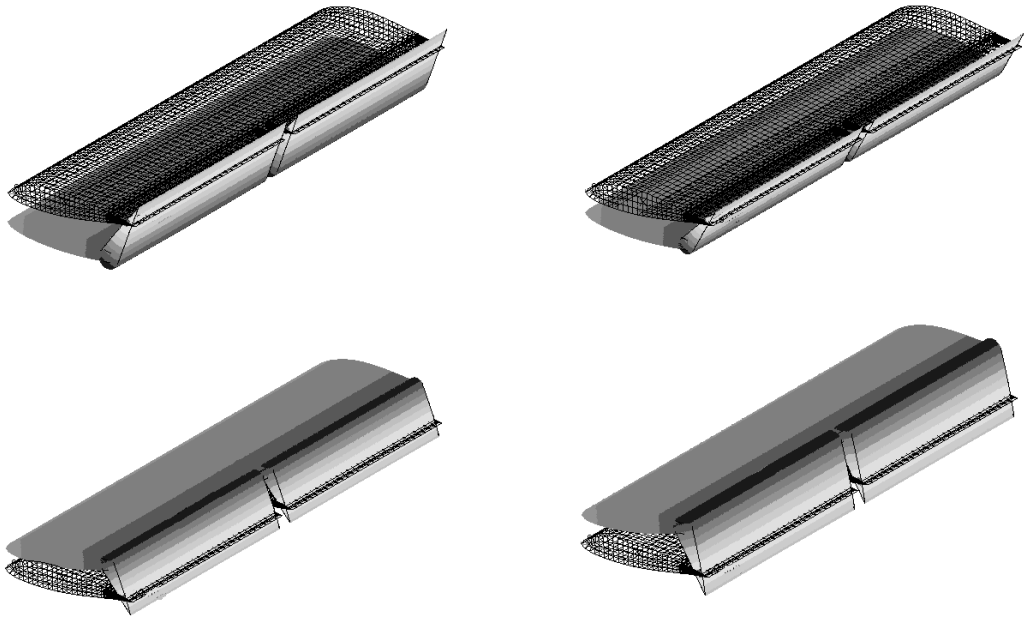

Figure 8. Four snapshots of flutter mode over a half-cycle

pitch modes are clearly visible at 2.6 Hz and 6.7 Hz, respectively. The acceleration of one of the two flaps is used as sensor. The two curves visible in Figure 9 correspond to trailing edge tab deflection on the flap with the sensor and on the other flap. For frequencies up to 20.0 Hz, the responses are identical. This is to be expected as both plunge and pitch motion are symmetric with respect to the midplane of the wing section.

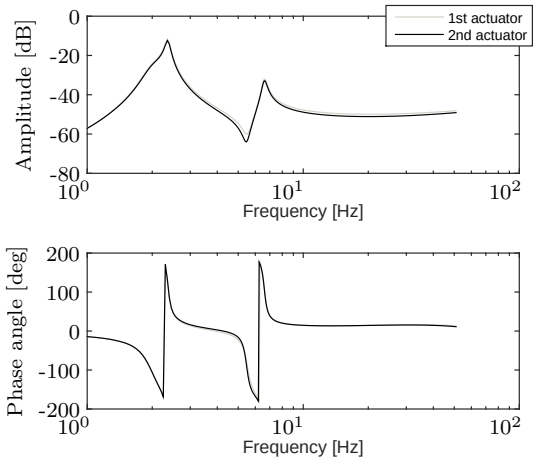

Figure 9. Transfer function of trailing edge tab deflection to plunge acceleration

The power requirements are driven by the tab operation. The estimated power consumption during operation is 10.5 mW per flap based on the aerodynamic moments that need to be overcome by each tab. Each generator can produce up to 70.0 mW at a nominal speed of 800 RPM, which is the average rotational speed in LCO with an amplitude of 5 degrees. This means that the system can operate 93% of the time in a control mode.

IV. Aeroelastic Time Domain Simulation of Autonomous Flap

An aeroelastic simulation has been performed to validate the design and the numerically demonstrate the feasibility of the concept. The aeroelastic time-domain simulation has been implemented in Simulink and re-uses the framework developed by Bernhammer et al.[11] The structural mode shapes are identical to the ones used to obtain the transfer function between tab input and flap response. The first 15 modes have been used as input to an aeroelastic analysis in ZAERO.[14] ZAERO was used to extract the aeroelastic state-space time-domain model based on the Minimum-State rational function approximation of the unsteady aerodynamic force coefficient matrices.[15] A modal damping coefficient of 0.057 is applied to the structural model, as identified by Sterenborg[12] for the test set-up. The aerodynamic model is divided into five zones, one for the wing section, one for each flap and one for each trailing edge tab. Figure 10 shows how the obtained state-space model is integrated into the Simulink simulations. A control feedback loop has been added. This feedback loop is additional to the non-linear feedback loops introducing the electromechanical moments and the forces generated by the structural delimiters.

Figure 10 also includes a gust input. The gust force time history in generalized coordinates has been computed in ZAERO for a continuous gust signal with a low turbulence intensity using a von Kármán turbulence spectrum for an altitude of 250 m above ground level. For the gust load cases, the gust forces are added to the equations of motion. The total state-space linear aeroelastic system is described mathematically in Equation 1. The state-space matrices, $\mathbf{A}$, $\mathbf{B}$, $\mathbf{C}$ and $\mathbf{D}$, the state vector, $\mathbf{x}$, and the input vector, $\mathbf{u}$, have been updated compared to the model of Bernhammer et al.[11] to include the control loop.

$$\begin{aligned} \dot{\mathbf{x}} = &\quad [\mathbf{A}]\,\mathbf{x} + [\mathbf{B}]\,(\mathbf{u} + \mathbf{u_{gust}}) \\ \mathbf{y} = &\quad\quad [\mathbf{C}]\,\mathbf{x} + [\mathbf{D}]\,\mathbf{u} \end{aligned} \tag{1}$$

with

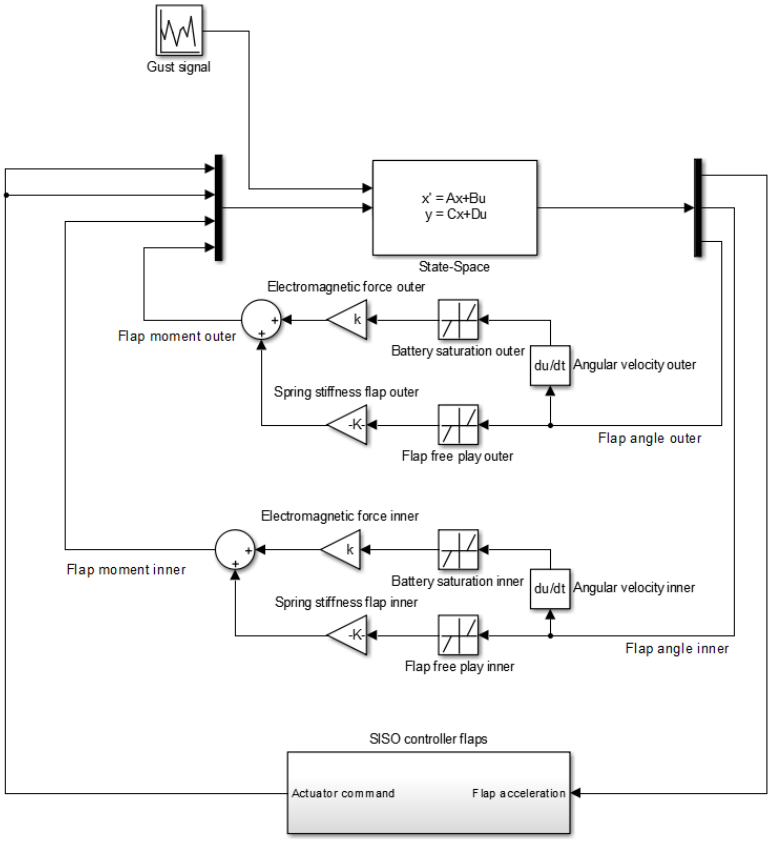

Figure 10. Simulink scheme of autonomous flap model

$$
\begin{aligned}
\mathbf{A} &= \begin{bmatrix} \mathbf{A_{ae}} & \mathbf{B_{ae}} & 0 \\ 0 & \mathbf{A_{ac}} & 0 \\ 0 & 0 & \mathbf{A_c} \end{bmatrix} \\
\mathbf{B} &= \begin{bmatrix} 0 & 0 \\ \mathbf{B_{ac}} & 0 \\ 0 & \mathbf{B_c} \end{bmatrix} \\
\mathbf{C} &= \begin{bmatrix} \mathbf{C_{ae}} & \mathbf{C_{ac}} & 0 \\ 0 & 0 & \mathbf{C_c} \end{bmatrix} \\
\mathbf{D} &= \begin{bmatrix} \mathbf{D_{ac}} & 0 \\ 0 & \mathbf{D_c} \end{bmatrix} \\
\mathbf{x} &= \begin{Bmatrix} \mathbf{x_{ae}} \\ \mathbf{x_{ac}} \\ \mathbf{x_c} \end{Bmatrix}
\end{aligned}
$$

The state vector, $\mathbf{x}$, contains the modal displacements and velocities, the aerodynamic lag, the actuator states and the control states, and the input vector, $\mathbf{u}$, contains the trailing edge tab commands and the non-linear feedback hinge moments. The vector $\mathbf{u_{gust}}$ contains the gust time history. The subscripts *ae* denote the aeroelastic model, *ac* the actuator and *c* the controller.

The electromagnetic resistance moment of the flap, which is introduced as part of the non-linear feedback hinge moment in the input vector $\mathbf{u}$, is modeled based on the electrical power of the generator. It is a function

of the rotational velocity. The magnitude of the moment can be computed based on Equations 2 and 3. The generated voltage, U, has to overcome the voltage of the battery, U_{bat}. Assuming no power loss over the rectifier, this can be separated into two cases.

$$U = \begin{cases} nl\frac{d\gamma}{dt} - U_{bat} & U_{open} > U_{bat} \\ 0 & U_{open} \leq U_{bat} \end{cases} \tag{2}$$

The electrical power, which is generated by the harvesting device, equals the mechanical power that is required to generate it. A resistance moment is applied to the state-space model to account for this power, which can be computed by:

$$P = \frac{\left(nl\frac{d\gamma}{dt}\right)^2}{R_{coil} + R_{var} + j\omega L_i} \approx \frac{(nl\gamma_k)^2}{R_{coil} + R_{var}}\dot{\beta}^2 \tag{3}$$

where β is the flap deflection angle. The magnetic flux gradient, $\frac{d\gamma}{dt}$, has been approximated by a constant value for $(nl\gamma_k)^2$ and the rotation speed of the flap. The constant for the magnetic field strength has been determined by matching the generated voltage during the wind tunnel experiment. The approximation of the term $(nl\phi_k)^2$ has a value of 9.1mNms/rad and a gear ratio of 80 is applied. The resistance in the loop $(R_{coil} + R_{var})$ is chosen to be 75Ω, which corresponds to the impedance matching condition. The structural stiffness outside the free-play zone is 3800Nm/rad and the width of the free-play zone is 17 degrees in both directions, again corresponding to the experimental results.

The mechanical moments, which add to the structural damping, are implemented in generalized coordinates into the state-space system together with a structural free-play zone as shown in Figure 10. The outputs of the state-space system are the plunge acceleration of the wing section and the rotation angles of both free-floating flaps. The rotational velocities are also obtained as output of the aeroelastic state-space system and serve as input to Equation 3.

V. Model Identification and Controller Design

In order to use the tabs to control structural vibrations, a feedback controller had to be designed. This was done in two steps: first, system identification was used to arrive at a dynamic model of the system. Next, classical loop-shaping techniques were used to design a controller that was capable of damping the plunge dominated vibrational mode of the system.

A. System Identification

One of the requirements for the design of a classical feedback controller was a simple dynamic model of the system to be controlled, preferably in terms of linear differential equations. Such a model may be obtained from first principles and physical modelling, which typically requires high accuracy in experiment construction and calibration. With structural and aerodynamic non-linearities, the complexity of such physical models often renders them challenging for the purpose of controller synthesis. Further, they may involve dynamics that are irrelevant within the controller bandwidth.

An alternative approach to obtain a controller-relevant system model is to use system identification techniques, such as subspace identification.[16] In such a method, experimental data is obtained by exciting the system and the input-output data is used directly to estimate a dynamic system model that can be used for controller design. Trim tab deflection was used for input data and the accelerometer mounted on the side plate provided the feedback control signal during the system identification process. A decision was taken to change the location of the accelerometer compared to the numerical study, as the accelerometer mounted on the side plates was delivering a measurement signal with a significantly higher signal-to-noise ratio than the accelerometers in the flaps. Consequently, system identification with less polluted data could be performed.

To simplify the identification problem, the identification experiment was conducted at a single wind speed (12.5 m/s), which is below the flutter speed. Due to friction in the flap mechanism of the wind tunnel model,

the flutter speed increased compared to the numerical studies from 11 2/s to roughly 13.0 m/s. The exact flutter point could not be determined as the damping of the aeroelastic apparatus was highly non-linear for small vibration amplitudes. Once a vibration amplitude threshold was overcome, the structural damping coefficient approached a value of 0.057, which was used in the numerical study.

The wing section was excited by applying a pseudo-random binary sequence of tab deflections, which resulted in structural oscillations, which were measured by the accelerometer located on the side plates. The acceleration measurement was used as input for the controller.

A transfer function $G(s)$ was estimated which describes the dynamics from the tab actuation angle β to the accelerometer response a_y, using the PBSID system identification technique.[17]

$$a_y = G(s)\beta. \tag{4}$$

The frequency-domain representation of the identified system is given in Figure 11. The grey line is the actual frequency-domain data obtained from the experiment, while the black line shows an estimate of the underlying state-space system. As expected, a resonance peak at the first structural mode of 3.0 Hz was clearly identified in the system identification experiment. While the frequency of the unstable branch of the numerical model decreases from the natural frequency of 3.0 Hz to 2.6 Hz when approaching the flutter speed as shown in Figure 7, the experiment did not exhibit this behaviour. Only a slight decrease in frequency from 3.0 Hz to 2.9 Hz was observed. Using this identified model, a classical feedback controller was designed for the system.

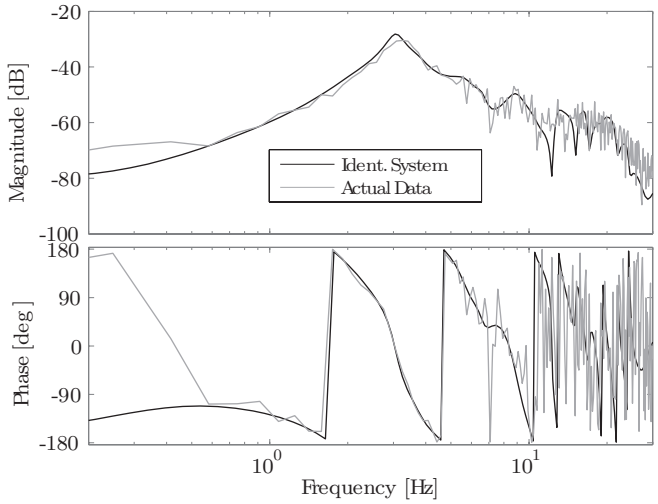

Figure 11. Bode plot of identified system at 12.5 m/s

B. Controller Design

The structural vibrations measured by the accelerometer were fed back to the controller, which generated the appropriate tab actuation signal to counteract and, thereby, damp the vibrations. Hence, there were three major considerations for the controller:

- There must be adequate gain around the first mode frequency of 3.0 Hz to be able to achieve feedback control.
- The actuation signal generated at the resonance frequency must produce an anti-phase structural response so that the vibrations are attenuated and not enhanced.
- The resulting closed-loop system must be stable.

Taking these considerations into account, a feedback controller $K(s)$ was designed that consisted of the following three elements:

$$K(s) = K_1(s)K_2(s)K_3(s), \tag{5}$$

where $K_1(s) = k$ is a simple gain, $K_2(s)$ is a phase lead compensator and K_3 is an inverted notch. The filter K_2 adds an adequate amount of phase within the bandwidth to achieve the right amount of damping,

$$K_2(s) = \frac{s/\omega_1 + 1}{s/\omega_2 + 1}, \tag{6}$$

and K_3 enhances the feedback at a single frequency, which is the same as the resonance frequency $\omega_r = 3.0$ Hz:

$$K_3(s) = \frac{(s/\omega_r)^2 + 2(s/\omega_r) + 1}{(s/\omega_r)^2 + 2\zeta(s/\omega_r) + 1}. \tag{7}$$

The various tuning parameters in the controller equations are detailed in Table 3.

Table 3. Control parameters: wind tunnel experiment

Parameter	Symbol	Value
Controller gain	k	3.333
Phase lead start frequency	ω_1	0.001 Hz
Phase lead end frequency	ω_2	0.5 Hz
Resonant frequency	ω_r	3.0 Hz
Notch damping	ζ	0.5

When this controller was connected in closed loop with the plant, the structural resonance peak was damped to a large extent, as can be seen in Figure 12. Figure 12 also shows a comparison to the numerical model in both cases 0.5 m/s below flutter speed. In the experiment, the acceleration measurement had been shifted to the pitch axis of the wing section instead of being located in the flaps. Therefore the accelerometer did not capture the flap deflection modes at 1.6 Hz or the pitch mode at 6.8 Hz, which are present in the original data. The amplitude of the plunge mode was almost exactly matched in the numerical model and the experiment. A shift in frequency of the mode, however, was observed between the experimental system identification and the numerical prediction. In the experiment the frequencies did not show the same drop with increasing wind speed as is observed in Figure 7 for the unstable branch around the flutter point.

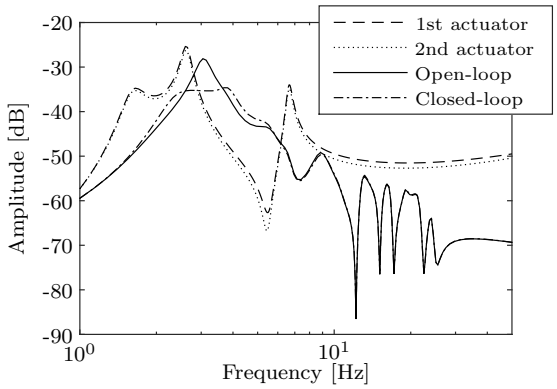

Figure 12. Bode plot of open-loop and closed loop system at 12.5 m/s (experiment: open and closed) and 10.5 m/s (numerical model: actuators)

The increased damping of the closed-loop system can also be seen in the time-domain results shown below, where the eigenmode oscillations decay much faster when the controller is active as shown in Figure 13.

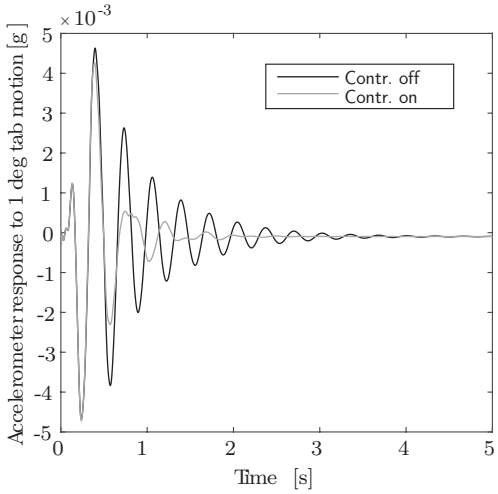

Figure 13. Decay of oscillation: Open-loop versus Closed-loop

C. Controller adaptation for numerical simulation

As explained in Section IV, the numerical aeroelastic model has been updated compared with the methodology of Bernhammer et al.[11] to include a control loop. The controller architecture used for the numerical simulations is analogous to the controller used in the wind tunnel experiment as presented in the previous subsection. While in the experiment, the plunge frequency remained constant for all wind speeds, numerically a drop in the frequency of the plunge mode has been observed from 3.0Hz at a wind speed of 0.0 m/s to 2.3 Hz at 11.0 m/s, which is the flutter speed. The notch filter in the controller design has been scheduled to match the frequency at the given wind speed. The control parameters used in the numerical simulation are provided in Table 4. It should be noticed that the controller gain has been adapted as well for the numerical simulations. This was needed because the controller input in the numerical simulation is the acceleration in terms of the gravitational constant, while in the experiment, the controller input is the measured accelerometer voltage.

Table 4. Control parameters: numerical simulation

Parameter	Symbol	Value
Controller gain	k	0.0016
Phase lead start frequency	ω_1	0.001 Hz
Phase lead end frequency	ω_2	0.5 Hz
Resonant frequency	ω_r	scheduled with wind speed
Notch damping	ζ	0.5

VI. Limit Cycle Oscillation

As is pointed out in the introduction, for the energy harvesting it is vital to be close to, or above, the flutter speed. For that purpose, limit cycle oscillations were studied intensively during the experiment. Two different types of limit cycles were investigated, namely structurally limited cycles and limit cycles that were achieved through control of the trailing edge tab.

A. Structurally Delimited Oscillations

The structural limit was achieved by constraining the flap deflection to remain within -20 and +30 degrees. Figure 14 shows the structurally limited oscillations in the wind tunnel experiment. The trailing edge tabs were used to initiate the vibration. The vibration amplitude increases as the system is operated in flutter until a limit cycle is reached. For small oscillation amplitudes, the system was still stable as a result of non-linear damping of the spring system. Then the controller is switched on and the vibration is damped out.

A sinusoidal oscillation with a frequency of 3.0 Hz was imposed on the trailing edge tab after 7.0 seconds. This oscillation immediately caused the flap to vibrate at the input frequency. A time delay of 1.0-1.5 seconds was observed when comparing the flap oscillations and the acceleration of the plunge mode. This time delay was caused by the inertia of the wing section, which only slowly started to oscillate. Practically at the same time as the accelerometer, the load cells, which were connected to the springs, showed an oscillation in the force measurements. In contrast to the load cells, which measured an almost perfect sinusoidal signal, the accelerometers measured a dominant signal of identical frequency, but their signal also show higher frequency components. The damping of the spring system might have reduced the amplitude of higher harmonics in the measurements of the vertical forces by the load cells.

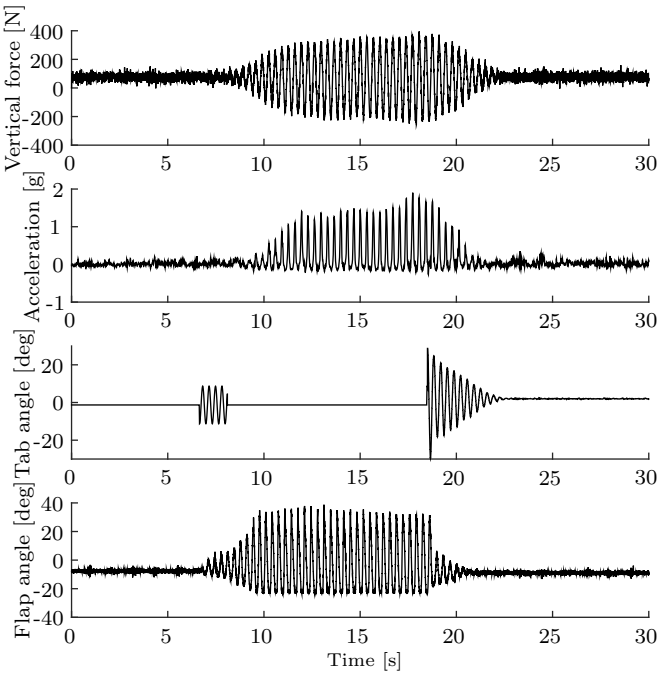

Figure 14. Structurally limit cycle oscillation

From 7.5 seconds until 18.0 seconds the system was unstable and the excitation signal was deactivated. At 9.0 seconds the flap deflection reached the delimiters of the flap, which caused a limit cycle oscillation. At 18.0 seconds the controller was switched on. Almost instantaneously, the amplitude of flap deflections reduced to 10 degrees, from which point it slowly decayed. This shows the stabilization effect the trailing edge tabs have on the flaps. The oscillations of the entire wing system decayed slower and reached a static position at 22.0 seconds.

B. Controlled Limit Cycle Oscillations

The second possibility to achieve limit cycle oscillations is to actively use the controller to limit the cycle amplitude. An identical test procedure was followed as described in the previous subsection, except that the controller was modified to include an on/off condition. This way the controller was only active if the flap amplitude in the previous oscillation cycle exceeded the specified threshold. The initialization of the limit cycle was identical to the previously described structurally limited oscillations. A sinusoidal oscillation was imposed as seen in the second subfigure of Figure 15. Again, the oscillations continued to grow after

the excitation signal was stopped. Flutter caused the oscillations to increase until the flaps reached their structural limits. This oscillation was maintained until the controller was activated at 11.0 seconds. The controller reduced the amplitude of the oscillations, but the high inertia of the plunge mode caused its oscillations to decay slowly. In that phase the controller was mostly active until the system reached a steady state. Around 17.0 seconds a stable pattern developed and the controller was only active 11% of the experimental time. The control activity almost immediately eliminated the vibration of the flaps. For three to four cycles, the controller stayed inactive, while the flap vibrations rebuilt. When flap vibrations exceeded the specified limit, the controller was reactivated until the vibrations decayed below this limit. The inertia of the system caused the accelerations of the wing section to decay much slower than the flap deflections when the controller was active. Thus, a practically constant limit cycle oscillation was reached at a lower amplitude, with a maximum flap deflection of 15 degrees.

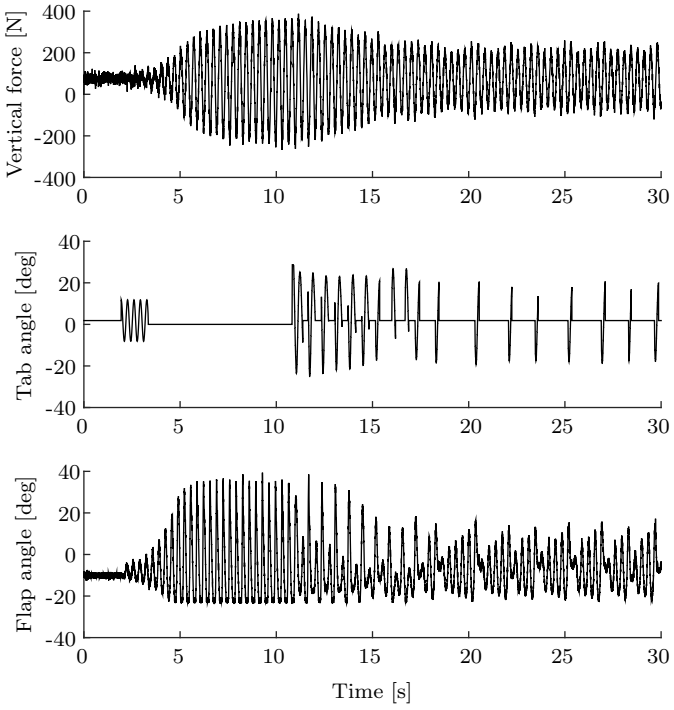

Figure 15. Controlled limit cycle oscillation

VII. Power Balance

The second task of the autonomous, free-floating flap is to generate enough power in order to be self-sustained. As mechanical friction in the gearbox and in the generator was high, the power that was generated by the flaps could not directly be measured. The observed mechanical friction stems primarily from the downsizing of the system to a wind tunnel size as small generators need higher rotational velocities than large generators and hence a high-ratio gearbox was necessary to couple the flap with the generator. A doubling of the generator diameter allows for doubling of the number of poles and, therefore, for a reduction of the rotational velocity to generate sufficient power. As a collateral effect of increasing the rotational velocity by a factor of 80 (the gear ratio), the apparent frictional torque on the flap was also increased by a factor of 80. Moreover, the low test speeds in the wind tunnel drastically reduced the aerodynamic moment that could be generated to overcome these forces.

The measurements presented in Figure 16 have been obtained by imposing a flap oscillation at the first flutter frequency to mimic the flap vibrations during limit cycle oscillations. As can be seen in the first subfigure of Figure 16, the frequency of the power signal was much higher than the flap oscillation frequency of 3.0 Hz. This was a result of the gear ratio and the number of poles. The power signal shows a high noise component. The source of the noise was mechanical friction in the rotation due to which a smooth rotation

could not be achieved and peaks and troughs in the rotational speed were observed. The power that could be reached in the presented configuration was measured over a resistance of 35.0 Ω. Figure 16 displays the sum of all four generators that have been installed in the aeroelastic apparatus. The root mean square power that could be achieved during the equivalent limit cycle oscillations is 564.0 mW.

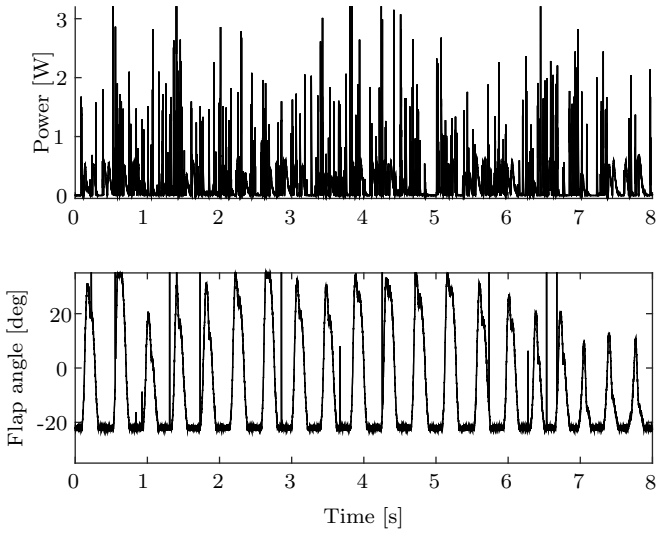

Figure 16. Power production of generators during sinusoidal oscillation at 3.0 Hz

The harvested energy should be sufficient to power the actuators and the accelerometers. The latter has a very low power requirement of less than 1 mW. Therefore, in practice the power requirements are primarily driven by the trailing edge tab actuators. Figure 17 shows an overview of the power consumption of all actuators. The top subfigure displays the current that was drawn for the actuator motion. The actuation system was powered by an external constant voltage source. The voltage that was supplied is shown in the middle subplot of Figure 17. Up to 4.0 Hz, the voltage demand could be matched exactly. Above this frequency, a drop in voltage output was observed, however the tabs still remained operational. This limitation could be circumvented if the amplitude of the tab rotation or the operational frequency were limited or the power supply and the servo actuators better matched.

The biggest share of the power consumption stemmed from operating the actuators themselves, namely from overcoming the friction and inertia in the actuator's drive train. The additional power requirement due to aerodynamic loads was small compared to the free oscillation, which can be observed in the lower subfigure. This curve includes the difference in power consumption for all actuators combined. Around 3.0 Hz, this difference was highest at just above 0.4W. At higher frequencies, the power source failed to deliver the demanded power. In the case of free oscillation of the tab and in the case of the loaded flap, the maximum power was drawn, such that the difference between both cases amounted to 0 W. One needs to bear in mind that the actuators only needed to be active 11% of the time to achieve a constant limit cycle amplitude. The averaged power consumption due to aerodynamic resistance moments therefore dropped to 0.0427 W, which is 14% of the generated power. When including the actuator power requirements, the average consumption increased to 0.440 W, which is 41% higher than the power production, however the actuators were overdimensioned for the size of the trailing edge tabs used in the experiment. Each trailing edge tab could be controlled with sufficient bandwith and amplitude even if one of the actuators were to fail.

VIII. Comparison between Numerical and Experimental Results

A. Limit cycle oscillation

The controller design used in the experiment has been tuned to the numerical simulation to account for the frequency shift as described before. Figure 18 displays the time history of the limit cycle oscillation and the subsequent controller activity. The results aim to reproduce the experimental counterpart, which is presented in Figure 14. In contrast to the experiment, the vibration in the numerical results is not initiated

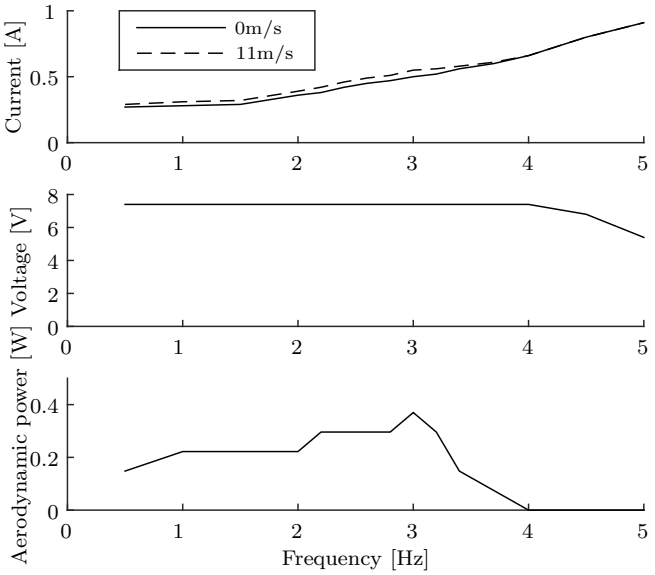

Figure 17. Power consumption of actuation system as function of actuation frequency and wind speed for 20 degrees tab amplitudes

by tab activity, but by a small initial deflection of the plunge mode that yields identical LCO. Perturbing the aeroelastic system post flutter speed leads to a diverging motion until the flaps reach their structural limit. When the controller is activated after 5.0 seconds, the system stabilizes and the vibrations damp out. The time scale in the numerical simulation associated to the damping is longer than in the experiment. This can be attributed to the lower tab deflections with a maximum of 10 degrees, while in the experiments, the maximum values reached were up to 20 degrees. This results in a lower damping of the flap motion and consequently a longer decay time.

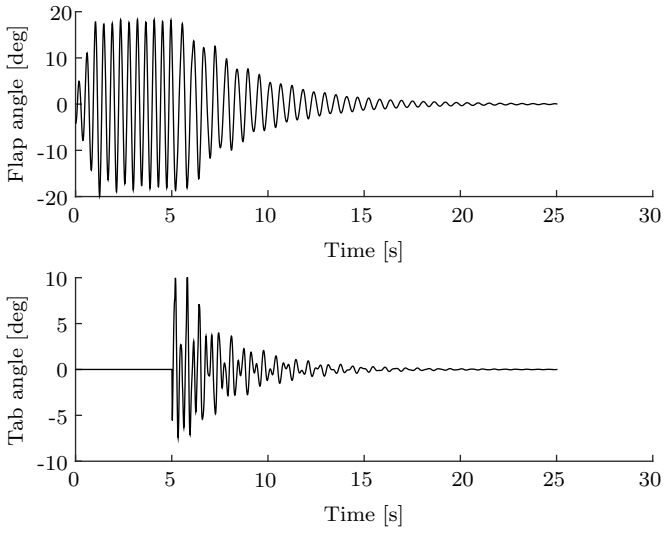

Figure 18. Structural limit cycle and active control

The second comparison study concerns the controlled limit cycle through tab activity. The numerical results are shown in Figure 19. The corresponding experimental results are presented in Figure 15. The numerical procedure is identical to the methodology for obtaining Figure 18, except that a controller on/off condition is included based on the recent time history of the flap oscillation amplitude. Figures 19 and 15 are similar until the first time the controller is switched off because the flap oscillation amplitude has dropped below 10 degrees. The controller activity causes the flaps to enter a stable limit cycle with a flap amplitude

of 10 degrees, similar to the experimental results (Figure 15). However, two differences in the results can be observed. The first difference is that the control activity during the experiment causes an immediate drop in flap oscillation amplitude from 15 to 5 degrees, while in the numerical simulation this drop is much lower. The reason is again, that the tab deflections set by the controller are around 10 degrees, while in the experiment they reach 20 degrees. The result is a more continuous control activity. In the experiment the time fraction, the controller was active, was 11%, while in the numerical simulations this time fraction is above 60%. The energy requirements on the flap are however lower, as the power consumption of the flaps is proportional to the rotational velocity of the tab and the aerodynamic forces on the flap, which are proportional to the amplitude when assuming that the lift is a linear function of the angle of attack. Decreasing the tab amplitude by a factor of 4 would yield a decrease in actuation requirements by a factor of 16.

The second difference is that the repetitive pattern observed in the experimental results is not reproduced by the numerical simulation. In the experiments, the strong drop in flap amplitude caused by control activity, recovered over several cycles before the amplitude exceeds the specified limit. Due to the small drop in flap oscillation amplitude in the numerical simulations, the oscillation grows to the specified amplitude within a single cycle.

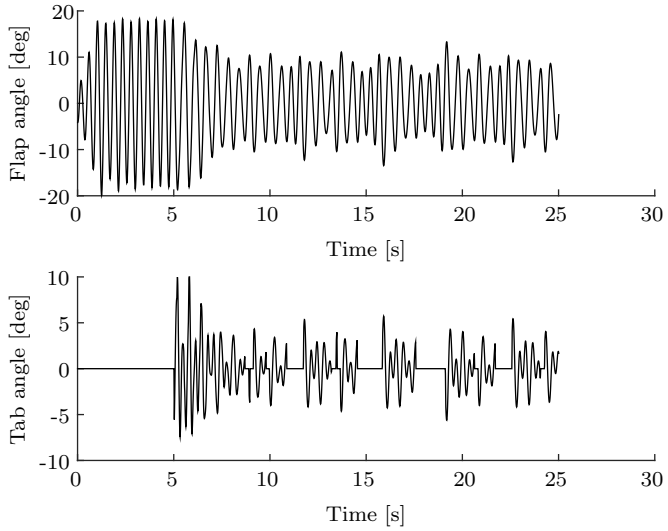

Figure 19. Limit cycle structure and control

B. Numerical simulation of power production

In a final step, the power production of the autonomous flap system has been analyzed. Figures 20 and 21 show the time history of flap rotation and voltage production. The voltage provided in Figure 21 is the sum of the voltages of all four generators as if they were connected in series. For the wind speeds of 3 m/s, 8 m/s and 10 m/s, the autonomous flap behavior remains stable. At wind speed of 12 m/s the flap is operating past the flutter point. In the first three operating conditions on a small voltage is being produced at the beginning, due to the vibrations introduced by the initial conditions. For wind speeds of 3.0 and 8.0 m/s, controlled and uncontrolled results are identically damped. At 10.0 m/s the flap deflection amplitude reaches 7.5 degrees at which point the controller becomes active for a very short period, which causes the results with and without controller to be different. For 12.0 m/s the open-loop results are confined by the structural limit, while in the closed-loop case, the controller sets the limit cycle amplitude.

The flap vibrations are converted into electrical energy. The fraction of the extracted energy is small, such that the electromechanical damping effect remains negligible. Due to the lower amplitude of the controlled limit cycle, the voltage output of the system is reduced in the closed-loop case.

In a final step, the average power production using different limit cycle amplitudes was computed for a range of wind speeds. During the experiment, a mean power per flap of 564.0 mW was produced. Figure 22 shows the total power of both flaps combined due to the initial conditions with a small amplitude in plunge mode. The time results include the incremental phase of the oscillation, such that the actual power

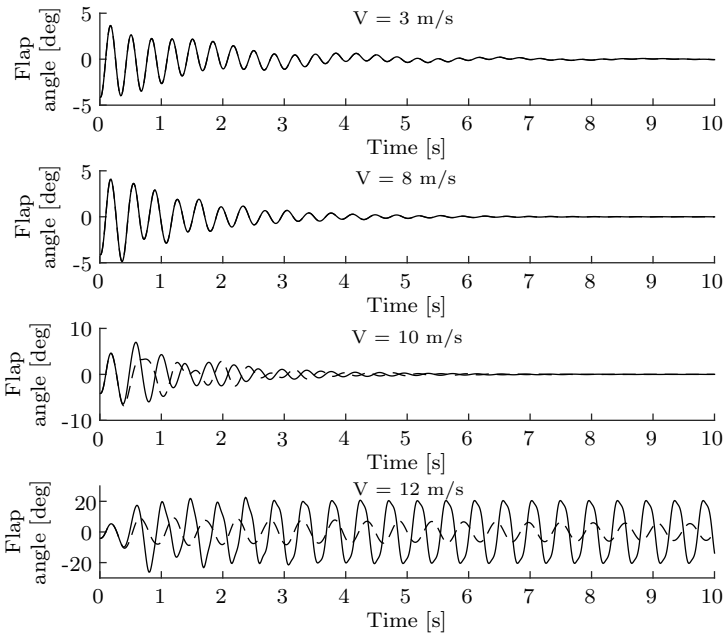

Figure 20. Rotation angles open (-) and closed loop (- -)

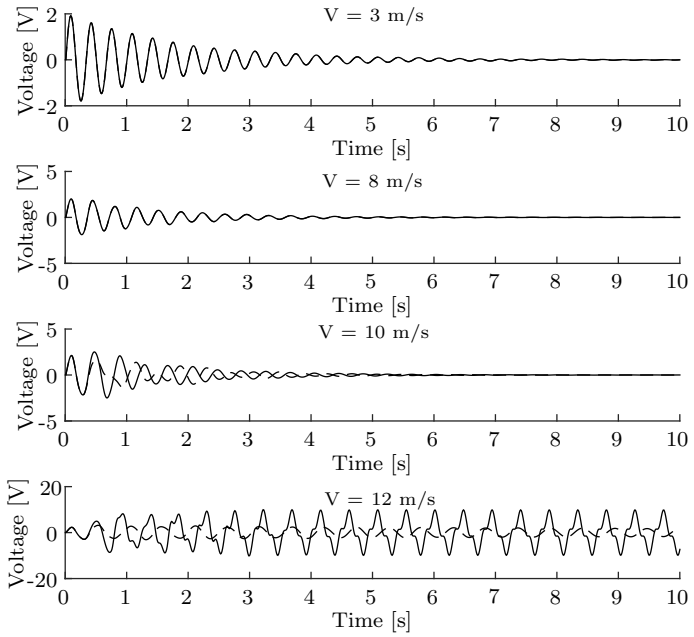

Figure 21. Voltage open (-) and closed loop (- -)

production during LCO, certainly for 11.0 m/s, which is only slightly unstable, will be slightly higher. By far the highest power production is achieved for the structural limit cycle. For a wind speed of 12.0 m/s a value of 510.0 mW is reached, which corresponds well with the experiment, certainly when considering that the LCO production in the numerical simulation should be slightly higher than the reported experimental value. The controlled limit cycles with an amplitude of 10 degrees produce 111 mW, while for 5 degrees, the average power is 29 mW.

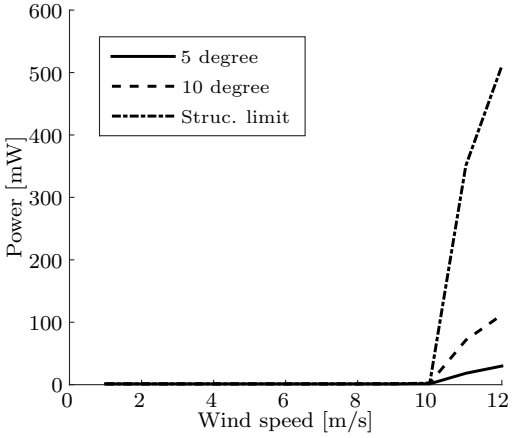

Figure 22. Power production of generators due to an initial impulse

IX. Conclusion

In this paper the concept of an autonomous, free-floating flap has been presented and a wind tunnel model designed. The flap system was retrofitted into an aeroelastic plunge and pitch apparatus. Numerically, the flutter speed was predicted to be 11.0 m/s, but due to friction in the flap system, the flutter speed was 13.0 m/s during the experiment. Two autonomous flaps were installed on a wing section. Each system included two actuators, two generators and an accelerometer. Additional sensors such as load cells were installed on the frame.

During the experiment, the transfer function of the tab command to an accelerometer command was identified. The obtained model agreed well with the numerical model, except for a drop in frequency of the numerical model close to the flutter speed, which was not observed during the experiment. It was experimentally shown that the system flutters in a combination of plunge and deflection motion. This flutter was successfully transformed into limit cycle oscillations using structural delimiters and by actively controlling the trailing edge tabs. The latter yielded a lower limit cycle amplitude than the structurally delimited oscillations. The energy harvester generated an average power of 564.0 mW, while the system consumed 42.7 mW. Therefore, the autonomous flap system is self-sufficient.

The experimental campaign has confirmed the findings of the numerical study. The major difference between simulation and experiment lies in the control activity, which was lower in the numerical model than in the experiment. Therefore, damping of the flap caused by the trailing edge tab was reduced compared to the experimental study. The result is a more continuous control activity with lower power requirements.

Acknowledgments

This research has been funded by the Far and Large Offshore Wind (FLOW) project of the Dutch Ministry of Economic Affairs.

References

[1]Heinze, S. and Karpel, M., "Analysis and wind tunnel testing of a piezo-electic tab for aeroelastic control applications," *Journal of Aircraft*, Vol. 43, No. 6, 2006, pp. 1799–1804.

[2]Bernhammer, L. O., De Breuker, R., Karpel, M., and van der Veen, G. J., "Aeroelastic Control Using Distributed Floating

Flaps Actuated by Piezoelectric Tabs," *Journal of Aircraft*, Vol. 50, No. 3, 2013, pp. 732–740.
[3]Pustilnik, M. and Karpel, M., "Dynamic Loads Alleviation Using Active Free-Floating Flaps," *Proceedings of the 53rd Israel Annual Conference on Aerospace Sciences*, Haifa, Israel, 2013.
[4]Pustilnik, M. and Karpel, M., "Loads, Vibration and Maneuver Control Using Active Floating Flaps," *Proceedings of International Forum on Aeroelasticity and Structural Dynamics*, Royal Aeronautical Society, Bristol, UK, 2013.
[5]Bryant, M. and Garcia, E., "Modeling and Testing of a Novel Aeroelastic Flutter Energy Harvester," *Journal of Vibration and Acoustics*, Vol. 133, 2011, pp. 011010–1:10.
[6]Bryant, M., Fang, A., and Garcia, E., "Self-powered smart blade: helicopter blade energy harvesting," *Proceedings of the SPIE*, Vol. 7643, 2010, pp. 764317–1:10.
[7]Park, J., Morgenthal, G., Kim, K., Kwon, S., and Law, K. H., "Power Evaluation for flutter-based Electromagnetic Energy Harvester using CFD Simulations," *Proceedings of the First International Conference on Performance-based and Life-cycle Structural Engineering*, Hong Kong, China, 2012.
[8]Park, J., Kim, K., Kwon, S., and Law, K. H., "An aero-elastic flutter based electromagnetic energy harvester with wind speed augmenting funnel," *Proceedings of the International Conference on Advances in Wind and Structures*, Seoul, Korea, 2012.
[9]Bruni, C., Cestino, E., Frulla, G., and Marzocca, P., "Developement of an aeroelastic wing model with piezoelectric elements for gust load alleviation and energy harvesting," *Proceedings of the ASME 2014 International Mechanical Engineering Congress and Exposition*, Montreal, Canada, 2014.
[10]Sirohi, J. and Mahadik, R., "Piezoelectric wind energy harvester for low-power sensors," *Journal of Intelligent Material Systems and Structures*, Vol. 22, No. 18, 2011, pp. 2215–2228.
[11]Bernhammer, L., Karpel, M., and De Breuker, R., "Energy harvesting for actuators and sensors using free-floating flaps," *Journal of Intelligent Material Systems and Structures*, Vol. accepted, 2015.
[12]Sterenborg, J., *Experimental and numerical investigation of an aeroelastic wing*, TU Delft, Delft, Netherlands, 2014, Ph.D. Thesis.
[13]Rodden, W. and Johnson, E., "MSC Nastran Aeroelastic Analysis User's Guide," MSC Software Corporation USA, 1994.
[14]Zona Technology, "ZAERO Theoretical Manual," Scottsdale, USA, 2011.
[15]Karpel, M., "Time Domain Aeroservoelastic Modeling UsingWeighted Unsteady Aerodynamic Forces," *Journal of Guidance, Control and Dynamics*, Vol. 13, 1990, pp. 30–37.
[16]Verhaegen, M. and Verdult, V., *Filtering and System Identification: A Least Squares Approach*, Cambridge, UK, Cambridge University Press, 2007.
[17]Chiuso, A., "The role of vector auto-regressive modelling in predictor based subspae identification," *Automatica*, Vol. 43, 2007, pp. 1034–1048.